Time-Dependent Multilevel Density Functional Theory

Tommaso Giovannini,*,† Marco Scavino,† and Henrik Koch*,‡

†*Scuola Normale Superiore, Piazza dei Cavalieri 7, 56126 Pisa, Italy.*

‡*Department of Chemistry, Norwegian University of Science and Technology, 7491 Trondheim, Norway.*

E-mail: tommaso.giovannini@sns.it; henrik.koch@ntnu.no

Abstract

We present a novel three-layer approach based on multilevel density functional theory (MLDFT) and polarizable molecular mechanics to simulate the electronic excitations of chemical systems embedded in an external environment within the time-dependent DFT formalism. In our method, the electronic structure of a target system, the chromophore, is determined in the field of an embedding inactive layer, which is treated as frozen. Long-range interactions are described by employing the polarizable fluctuating charges (FQ) force field. The resulting MLDFT/FQ thus accurately describes both electrostatics (and polarization) and non-electrostatic target-environment interactions. Robustness and reliability of the approach are demonstrated by comparing our results with experimental data reported for various organic molecules in solution.

1 Introduction

The modeling of electronic excitations of molecular systems embedded in an external environment is a challenging task in theoretical and computational chemistry. In fact, the large number of degrees of freedom to be considered makes the treatment of the whole system with quantum mechanics (QM) rapidly unfeasible. To face this problem, focused models have been proposed.[1–4] The system is divided into at least two interacting parts:[5–7] the target chromophore and the external environment. The computational advantages associated with such techniques rely on the different levels of sophistication employed to describe the two parts, assuming that the external environment acts as a perturbation on the chromophore, modifying but not determining its properties.[2] In this vision, the target system is generally described by means of accurate QM methodologies, while the environment is treated at a lower level of accuracy.[1–4]

The most used focused methods belong to the family of the so-called QM/classical approaches,[2–4,8,9] either continuum or atomistic, in which the environment is treated by means of classical physics. In these methods, the target-environment interaction is fully described at the classical level, generally by means of electrostatics. The great success of these approaches is mainly associated with their low computational cost, which is comparable to gas-phase calculations for a self-consistent field (SCF) wave function. In atomistic QM/molecular mechanics (QM/MM) methods,[3] the accuracy depends on the energetic terms describing the QM/MM interaction once the preferred QM level is selected. They are generally limited to electrostatics (and polarization in polarizable QM/MM approaches).[1–3,10] Non-electrostatics (van der Waals) is instead considered by means of parametrized functions, such as Lennard-Jones, although a few formulations in terms of the QM density also exist.[11–13]

To refine the description provided by QM/MM methods, quantum embedding can be exploited.[14–26] In these approaches, the system is generally divided into two parts, active and inactive, which are both treated at the QM level but at different levels of sophistication. Many quantum embedding methods have been proposed, ranging from frozen density

embedding[24,27–33] to projected-based approaches.[17,18,22,23,34,35] We have recently developed a novel quantum embedding based on density functional theory (DFT), named multilevel DFT (MLDFT),[36,37] which successfully partitions the system into active and inactive parts by decomposing the QM density matrix. Due to such partitioning, the problems related to the definition of non-additive kinetic energy in Frozen Density Embedding (FDE) can be avoided.[38] The approach is remarkably versatile and has been successfully applied to calculating solvation energies and hyperfine coupling constants in unrestricted formalism.[36,37]

Similarly to its analogous ML Hartree-Fock (MLHF),[39–42] the MLDFT methodology restricts the MO space to that spanned by the active MOs only, providing a large computational saving compared to full DFT calculations.[36,37] In this work, we exploit this feature to extend the method to calculate electronic excitations using the time-dependent (TD) DFT formalism.[43] To apply the method to real case systems, we couple MLDFT to a third classical MM layer, described using the polarizable fluctuating charge (FQ) force field,[44,45] which permits a proper description of long-range interactions at a reduced computational cost.[26] Furthermore, we introduce the modeling of active-inactive mutual polarization interactions in TD-MLDFT, which are needed to treat electronic transitions with large transition dipole moments.[26] In fact, similarly to most quantum embedding methods, in MLDFT, the inactive density (matrix) is kept frozen in the calculation; thus, the polarization relaxation of the inactive density is generally neglected. To deal with this problem, we reformulate in the TD-MLDFT/FQ context a recent approach proposed by some of the authors in the frozen density embedding (FDE) framework.[26] Within this approach, the polarization of the inactive layer in the response regime is modeled in terms of classical polarizable force fields, thus offering an effective yet cost-effective description of active-inactive mutual polarization.

The paper is organized as follows. In the next section, we describe MLDFT, its extension to TD formalism, and its coupling with a third polarizable FQ layer. After briefly discussing the computational details, we apply the developed approach to various solvated molecular systems characterized by electronic transitions of different natures. Some conclusions and

future perspectives are given at the end.

2 Theory

In MLDFT, the partitioning of the system into two parts is based on a decomposition of the total density matrix $\mathbf{D}$, and a similar separation in the density function $\rho(\mathbf{r})$ as well:[36]

$$\mathbf{D} = \mathbf{D}^A + \mathbf{D}^B \qquad \Rightarrow \qquad \rho(\mathbf{r}) = \rho^A(\mathbf{r}) + \rho^B(\mathbf{r}) \tag{1}$$

where A and B indicate the active and inactive fragments. The partitioning defined in Eq. 1 is not unique, and different methods to perform such a separation can be exploited. In this work, we use a partial Cholesky decomposition of the total density matrix for the active occupied molecular orbitals (MOs), from which the active density matrix $\mathbf{D}^A$ is calculated.[39,46–49] This approach ensures that all active and inactive MOs remain orthogonal during all the subsequent SCF procedures performed on the active subsystem.[50] By using eq. 1, the electronic energy of the system for a generic hybrid DFT functional can be written as:

$$E[\mathbf{D}^A;\mathbf{D}^B] = e[\mathbf{D}^A] + e[\mathbf{D}^B] + e^{AB}[\mathbf{D}^A;\mathbf{D}^B] \tag{2a}$$

$$\begin{aligned} e[\mathbf{D}^X] = {} & \mathrm{Tr}\mathbf{h}\mathbf{D}^X + \frac{1}{2}\mathrm{Tr}\mathbf{D}^X\mathbf{J}(\mathbf{D}^X) - \frac{1}{2}c_\mathrm{x}\mathrm{Tr}\mathbf{D}^X\mathbf{K}(\mathbf{D}^X) \\ & + (1-c_\mathrm{x})\int \rho^X(\mathbf{r})\varepsilon_\mathrm{x}(\rho^X(\mathbf{r}))\,\mathrm{d}\mathbf{r} \\ & + \int \rho^X(\mathbf{r})\varepsilon_\mathrm{c}(\rho^X(\mathbf{r}))\,\mathrm{d}\mathbf{r} \qquad \{X = A, B\} \end{aligned} \tag{2b}$$

$$\begin{aligned} e^{AB}[\mathbf{D}^A;\mathbf{D}^B] = {} & \mathrm{Tr}\mathbf{D}^A\mathbf{J}(\mathbf{D}^B) - c_\mathrm{x}\mathrm{Tr}\mathbf{D}^A\mathbf{K}(\mathbf{D}^B) \\ & + (1-c_\mathrm{x})\left(\int \rho^A(\mathbf{r})\varepsilon_\mathrm{x}(\rho^B(\mathbf{r}))\,\mathrm{d}\mathbf{r} + \int \rho^B(\mathbf{r})\varepsilon_\mathrm{x}(\rho^A(\mathbf{r}))\,\mathrm{d}\mathbf{r}\right) \\ & + \int \rho^A(\mathbf{r})\varepsilon_\mathrm{c}(\rho^B(\mathbf{r}))\,\mathrm{d}\mathbf{r} + \int \rho^B(\mathbf{r})\varepsilon_\mathrm{c}(\rho^A(\mathbf{r}))\,\mathrm{d}\mathbf{r} + E^{AB}_{\text{non-add}} \end{aligned} \tag{2c}$$

where $\mathbf{h}$ is the one-electron integrals, $\mathbf{J}$ and $\mathbf{K}$ are Coulomb and exchange matrices, respectively. ε_{x} and ε_{c} are the exchange and correlation energy densities per unit particle. The coefficient c_{x} defines whether pure DFT ($c_{\mathrm{x}} = 0$), or hybrid DFT functionals ($c_{\mathrm{x}} \neq 0$) are used. Note that if the SCF converged density matrix $\mathbf{D}$ of the full system is decomposed (Eq. 1), Eq. 2 yields the ground state DFT energy of the total system. In MLDFT, we do not minimize the energy at the full DFT level. Instead, we decompose an approximated density matrix for the total system, which is obtained by diagonalizing a Fock matrix constructed by using a density matrix guess (in this work, a superposition of molecular densities, vide-infra). The last term $E^{AB}_{\text{non-add}}$ originates from the non-linearity of ε_{x} and ε_{c}, and it is defined as:

$$\begin{aligned} E^{AB}_{\text{non-add}}[\mathbf{D}^A;\mathbf{D}^B] = (1-c_{\mathrm{x}}) \left(\int \rho(\mathbf{r})\varepsilon_{\mathrm{x}}(\rho(\mathbf{r}))\,\mathrm{d}\mathbf{r} - \int \rho(\mathbf{r})\varepsilon_{\mathrm{x}}(\rho^A(\mathbf{r}))\,\mathrm{d}\mathbf{r} - \int \rho(\mathbf{r})\varepsilon_{\mathrm{x}}(\rho^B(\mathbf{r}))\,\mathrm{d}\mathbf{r} \right) \\ + \int \rho(\mathbf{r})\varepsilon_{\mathrm{c}}(\rho(\mathbf{r}))\,\mathrm{d}\mathbf{r} - \int \rho(\mathbf{r})\varepsilon_{\mathrm{c}}(\rho^A(\mathbf{r}))\,\mathrm{d}\mathbf{r} - \int \rho(\mathbf{r})\varepsilon_{\mathrm{c}}(\rho^B(\mathbf{r}))\,\mathrm{d}\mathbf{r} \end{aligned} \tag{3}$$

In Eq. 2, the first four lines define the energy of the active and inactive fragments, whereas the last three lines define the active-inactive interaction. In MLDFT, the density matrix of the inactive part $\mathbf{D}^B$ (and $\rho^B(\mathbf{r})$) is frozen, and therefore it acts as an external field on the active fragment. Therefore, the energy terms containing the B labels are fixed during the SCF procedure. The total MLDFT Fock matrix is given by functional differentiation with respect to the active density only since the inactive density is kept frozen:[36]

$$
\begin{aligned}
F_{\mu\nu} &= h_{\mu\nu} \\
&+ J_{\mu\nu}(\mathbf{D}^A) - c_{\mathrm{x}} K_{\mu\nu}(\mathbf{D}^A) + (1 - c_{\mathrm{x}}) \int v_{\mathrm{x}}(\rho^A(\mathbf{r}))\chi_\mu(\mathbf{r})\chi_\nu(\mathbf{r})\,\mathrm{d}\mathbf{r} + \int v_{\mathrm{c}}(\rho^A(\mathbf{r}))\chi_\mu(\mathbf{r})\chi_\nu(\mathbf{r})\,\mathrm{d}\mathbf{r} \\
&+ J_{\mu\nu}(\mathbf{D}^B) - c_{\mathrm{x}} K_{\mu\nu}(\mathbf{D}^B) + (1 - c_{\mathrm{x}}) \int v_{\mathrm{x}}(\rho^B(\mathbf{r}))\chi_\mu(\mathbf{r})\chi_\nu(\mathbf{r})\,\mathrm{d}\mathbf{r} + \int v_{\mathrm{c}}(\rho^B(\mathbf{r}))\chi_\mu(\mathbf{r})\chi_\nu(\mathbf{r})\,\mathrm{d}\mathbf{r} \\
&+ (1 - c_{\mathrm{x}}) \int \chi_\mu(\mathbf{r})\chi_\nu(\mathbf{r})[v_{\mathrm{x}}(\rho^A(\mathbf{r}) + \rho^B(\mathbf{r})) - v_{\mathrm{x}}(\rho^A(\mathbf{r})) - v_{\mathrm{x}}(\rho^B(\mathbf{r}))]\,\mathrm{d}\mathbf{r} \\
&+ \int \chi_\mu(\mathbf{r})\chi_\nu(\mathbf{r})[v_{\mathrm{c}}(\rho^A(\mathbf{r}) + \rho^B(\mathbf{r})) - v_{\mathrm{c}}(\rho^A(\mathbf{r})) - v_{\mathrm{c}}(\rho^B(\mathbf{r}))]\,\mathrm{d}\mathbf{r}
\end{aligned} \tag{4}
$$

where, $v_{\mathrm{x}}(\rho(\mathbf{r}))$ and $v_{\mathrm{c}}(\rho(\mathbf{r}))$ are the exchange and correlation potential densities, respectively. Note that the two-electron terms associated with the B fragment act as a one-electron term since the associated density matrix is kept frozen.

To summarize, we remark on an important advantage of MLDFT as compared to full DFT, which is particularly useful in its extension to the time-dependent formulation. The MLDFT SCF procedure is performed on the MO basis of the active part only, thus intrinsically reducing the dimensionality of the problem and the associated computational time.[39]

2.1 Coupling with a third MM layer

To further increase the applicability of the MLDFT approach, we couple it with a third MM layer defined in terms of purely electrostatic embedding (fixed charges placed on each MM atom) or polarizable embedding.[3] Among the many polarizable embeddings,[13,51–53] in this work we exploit the polarizable fluctuating charges force field. In this method, each MM atom is endowed with a charge whose value varies as a response to the external potential and the differences in atomic electronegativities.[44,45,54,55] The energy of the resulting MLDFT/MM(FQ) reads:

$$
\mathcal{E} = E_{\mathrm{MLDFT}} + E_{\mathrm{MM}} + E^{\mathrm{int}}_{\mathrm{MLDFT/MM}} \tag{5}
$$

where E_{MLDFT} is given in Eq. 2, whereas E_{MM} and $E^{\mathrm{int}}_{\mathrm{MLDFT/MM}}$ are MM and MLDFT/MM interaction energies, respectively. For both non-polarizable MLDFT/MM or polarizable MLDFT/FQ, the interaction energy can be written as follows:

$$E^{\mathrm{int}}_{\mathrm{MLDFT/MM}} = \sum_i q_i V_i(\mathbf{D}) \tag{6}$$

where $V_i(\mathbf{D})$ is the electric potential generated by the total QM density matrix (i.e., both active and inactive contributions) on the i$-th$ charge (q_i). As stated above, for non-polarizable QM/MM, q_i values are fixed, whereas, in QM/FQ, they explicitly depend on the QM density and are obtained by minimizing the following energy expression:[37]

$$\begin{aligned}\mathcal{E}[\mathbf{D}_A, \mathbf{D}_B, \mathbf{q}, \boldsymbol{\lambda}] = & E_{\mathrm{MLDFT}}[\mathbf{D}_A, \mathbf{D}_B] \\ & + \frac{1}{2}\mathbf{q}_\lambda^\dagger \mathbf{M}\mathbf{q}_\lambda + \mathbf{q}_\lambda^\dagger \mathbf{C}_Q \\ & + \mathbf{q}_\lambda^\dagger \mathbf{V}(\mathbf{D})\end{aligned} \tag{7}$$

where $\mathbf{q}_\lambda$ indicates a vector collecting FQ charges and a set of Lagrangian multipliers, which ensure charge conservation on each fragment composing the MM layer (e.g., on each solvent molecule for solvated systems). The $\mathbf{M}$ matrix is the interaction kernel between the FQ charges, which also contains the Lagrangian blocks,[56] and the vector $\mathbf{C}_Q$ accounts for the interaction between permanent moments, i.e., χ and charge constraints Q on each FQ moiety. The FQ charges equilibrated for the MLDFT/FQ systems are obtained by minimizing the energy functional in Eq. 7. This procedure yields the following set of linear equations:

$$\mathbf{M}\mathbf{q}_\lambda = -\mathbf{C}_Q - \mathbf{V}(\mathbf{D}) \tag{8}$$

In parallel, the MLDFT/MM Fock matrix is defined as:

$$F_{\mu\nu} = F^{\mathrm{MLDFT}}_{\mu\nu} + \sum_i q_i V_{i,\mu\nu} \tag{9}$$

where $F_{\mu\nu}^{\mathrm{MLDFT}}$ is defined in Eq. 4. As for energy contributions, the additional QM/MM term is fixed and computed only at the first SCF cycle in the case of non-polarizable QM/MM, whereas it changes in QM/FQ because FQ charges depend on QM densities. Therefore, MLDFT/FQ contribution to the Fock matrix must be updated at each SCF cycle, ultimately introducing mutual polarization effects between MLDFT and FQ layers.[37]

2.2 Time-Dependent Multilevel Density Functional Theory

Besides calculating energy, MLDFT/FQ can be extended to compute molecular properties and spectroscopies, similar to other multilayer approaches.[26] Here, we focus on the excitation energies of embedded molecules by resorting to Time-Dependent Density Functional Theory (TD-DFT).[43] The extension of MLDFT/FQ to excited states needs to consider the response of the environment to the electronic excitation taking place in the target molecule, i.e., to the molecular density evolving in time as a result of the electronic excitation.[57] The treatment of such a contribution has already been formulated for the QM/FQ model by explicitly considering the FQ response to the molecular transition density.[56] In particular, in the linear response regime, FQ charges are adjusted to the transition density associated with the specific electronic excitation under examination.[56]

The standard way to calculate transition properties in DFT is to resort to TD-DFT.[43] In particular, TD-DFT equations in the Casida formalism read:

$$\begin{pmatrix} \tilde{\mathbf{A}} & \tilde{\mathbf{B}} \\ \tilde{\mathbf{B}}^* & \tilde{\mathbf{A}}^* \end{pmatrix} \begin{pmatrix} \mathbf{X} \\ \mathbf{Y} \end{pmatrix} = \omega \begin{pmatrix} \mathbf{1} & \mathbf{0} \\ \mathbf{0} & -\mathbf{1} \end{pmatrix} \begin{pmatrix} \mathbf{X} \\ \mathbf{Y} \end{pmatrix} \tag{10}$$

where $\tilde{A}$ and $\tilde{B}$ matrices are defined as:

$$\tilde{A}_{ai,bj} = (\epsilon_a - \epsilon_i)\delta_{ab}\delta_{ij} + (ai|bj) - c_{\mathrm{x}}(ab|ij) + c_{\mathrm{l}} f_{ai,bj}^{\mathrm{xc}} + C_{ai,bj}^{QM/FQ} \tag{11}$$

$$\tilde{B}_{ai,bj} = (ai|bj) - c_{\mathrm{x}}(aj|ib) + c_{\mathrm{l}} f_{ai,jb}^{\mathrm{xc}} + C_{ai,bj}^{QM/FQ} \tag{12}$$

where $(pq|rs)$ are two electron integrals, ε are the MO energies, and ω are the excitation energies. c_{x} and c_{l} are coefficients depending on the SCF level exploited ($c_{\mathrm{x}} = 1$, $c_{\mathrm{l}} = 0$ for HF wavefunctions, $c_{\mathrm{x}} = 0$, $c_{\mathrm{l}} = 1$ for pure DFT).

$C^{\mathrm{QM/FQ}}_{ai,bj}$ indicates additional contributions to the $\tilde{A}$ and $\tilde{B}$ matrices due to the presence of the FQ layer. Such terms are defined as:

$$C^{\mathrm{FQ}}_{ai,bj} = \sum_{p} \left(\int_{\mathbb{R}^3} \varphi_a(\mathbf{r}) \frac{1}{|\mathbf{r} - \mathbf{r}_p|} \varphi_i(\mathbf{r}) \, \mathrm{d}\mathbf{r} \right) \cdot q^T_p(\varphi_b, \varphi_i) \tag{13}$$

where p label the MM atoms, q^T are the perturbed charges (placed at positions $\mathbf{r}_p$), which are adjusted to the transition density $\mathbf{D}^T_K = \mathbf{X}_K + \mathbf{Y}_K$.[56] φ indicates occupied (i, j indexes) or virtual (a, b indexes) MO orbitals. In particular, they are obtained by solving the following linear set of equations:

$$\mathbf{M}\mathbf{q}^T_\lambda = -\mathbf{V}(\mathbf{D}^T) \tag{14}$$

which is the perturbed version of Eq. 8. The solution of the response equations in Eq. 10 yields excitation energies and transition amplitudes. In MLDFT, the fixed inactive density B response is not considered. In this formalism, the linear response of the active system is only indirectly affected by the inactive portion due to the modification of the active MOs solving the ground state equations (see Eq. 2). Therefore, in the MLDFT/FQ approach, the frozen density D^B only affects the MOs of the fragment A in the ground state, whereas the FQ response is adjusted to the transition density of the active portion only.

In this picture, the frozen layer separates the active and the FQ subsystems, which instead dynamically respond to the external time-dependent perturbation. This potentially yields an unphysical description of the phenomenon and can affect the computed results, in particular for those electronic transitions where the environmental response cannot be neglected. An alternative approach involves computing the response of the inactive layer through a coupled model,.[58–60] This means integrating the FQ response with the response functions

of both active and inactive regions, similar to the methodology proposed in the context of subsystem DFT.[58–60] We here adopt a different strategy, in parallel to that proposed by some of the present authors in the framework of the FDE/FQ method.[26] Specifically, only for the response equations the inactive atoms are endowed with FQs, and their response is computed using the same method exploited for the FQ layer. This involves modifying Eq. 13 to account for the charges of both the FQ and inactive atoms in the B region. We denote this method MLDFT$_{\mathrm{FQ}}$/FQ. This procedure ensures that the entire environment responds to external perturbation. At the same time, the dimensionality of the linear system in Eq. 10 is maintained, as the response of the static density layer is inherently included within the $\tilde{A}$ and $\tilde{B}$ matrices, rather than through explicit excitations. Note that the perturbed charges sum to zero on each FQ moiety; thus, there is no extra charge density introduced spuriously in the inactive MLDFT portion. Finally, we remark that the proposed procedure is general and can be applied to any environment, pending a reliable parametrization of the FQ force field.

Calculating the terms of Eq. 13 for both inactive and FQ layers is cost-effective; therefore, the overall cost of the calculation is not particularly affected. The novel MLDFT$_{\mathrm{FQ}}$/FQ combines the best aspects of quantum embedding methods and polarizable QM/MM approaches. In fact, it incorporates the effects of electrostatics, polarization, and quantum repulsion from the environment on the active system in its ground state. At the same time, such contributions are cost-effectively included in the response calculations. Note that Pauli repulsion is explicitly included in the GS and indirectly affects the excitation energies by modifying the GS MOs. This is consistent with other approaches proposed in the literature for describing Pauli repulsion effects on linear response.[12,13,26,28,61,62]

3 Computational Details

The TD-MLDFT$_{\mathrm{FQ}}$/FQ method is implemented in a development version of the electronic structure program e$^{\mathcal{T}}$.[63] As in Ref. 36, the DFT grid is constructed using the widely employed Lebedev grid,[64] with the radial quadrature proposed in Ref. 65. All the calculations are performed using a quadrature of 25$^{\mathrm{th}}$ order, and the radial threshold is set to 10^{-5}. The DFT functionals are implemented using the LibXC library.[66,67]

In this work, the TD-MLDFT$_{\mathrm{FQ}}$/FQ method is applied to the particular case of chromophores in solution. In all the reported calculations, a TD-MLDFT calculation is performed by following this computational protocol:

1. Construction of an initial density matrix by means of superposition of molecular densities.[27,68] The quantum region is partitioned into N_f fragments, i.e. the various molecules constituting active and inactive MLDFT parts (active molecule and the solvent molecules). For each fragment, the DFT energy is minimized in its own AO basis set, and the total density of the quantum region is then calculated as the direct sum of the fragment densities:

$$\mathbf{D} = \bigoplus_{i}^{N_f} \mathbf{D}_i \tag{15}$$

   In other words, the total density matrix is block-diagonal, and the blocks are the SCF-converged fragment density matrices. By using Eq. 15, an initial Fock matrix of the total system is constructed and then diagonalized to obtain an idempotent and physically consistent density matrix. Note that at this step, a part of the active-inactive polarization energy is introduced. Indeed, in previous works, we have shown that, for neutral species, the largest part of active-inactive polarization energy is taken into account by MLDFT.[36,37]

2. Partitioning of the new density matrix into A and B densities, by using a partial Cholesky decomposition for the active occupied orbitals.[42,49,50,69–71] The Cholesky decomposition of the total density $\mathbf{D}$ into $\mathbf{D}^A$ and $\mathbf{D}^B$ is unique if the same pivots are

used. In this work, the Cholesky decomposition is performed by selecting the diagonal elements corresponding to the basis functions, which are centered on the active atoms:[39,47,50]

$$\begin{aligned} D^A_{\alpha\beta} &= \sum_{IJ} D_{\alpha I} \tilde{D}^{-1}_{IJ} D_{\beta J} \\ &= \sum_{I} L_{\alpha I} L_{\beta I} \end{aligned} \tag{16}$$

where I and J are the diagonal elements which are decomposed, $\tilde{\mathbf{D}}$ is the submatrix of $\mathbf{D}$ containing the selected diagonals, and $L_{\alpha I}$ are the Cholesky orbitals. As a result of the decomposition, the active Cholesky MOs are obtained, and the active density matrix $\mathbf{D}^A$ is trivially constructed (see Eq. 16). The active virtual orbitals are instead constructed by means of projected AOs (PAOs), obtained from the AOs centered in the active fragment and orthonormalized through the Löwdin procedure.[72,73] The threshold for removing the linear dependencies is set to 10^{-6}. The inactive density $\mathbf{D}^B$ is finally obtained as the difference between the total $\mathbf{D}$ and the active $\mathbf{D}^A$ densities.

3. Calculation of the constant energy terms and the one-electron contributions due to the inactive density matrix B entering in Eqs. 2 and 4.

4. Minimization of the energy defined in Eq. 2 in the MO basis of the active part A only, until convergence is reached. All the equations reported in Section 2, expressed in the AO basis set, are transformed in the active MO basis using the active MO coefficients.

5. Solution of TD-MLDFT equations (Eq. 10). in the reduced active MO space. In the case of TD-MLDFT$_{\mathrm{FQ}}$/FQ calculations, all atoms of the inactive region are included in an enlarged FQ part, i.e. they are endowed with atomic electronegativities and chemical hardnesses. The FQ response matrix $\mathbf{M}$ (eq. 7) is thus reconstructed to include inactive and MM atoms, and Eq. 14 is solved to obtain the perturbed charges of both regions.

As a result of the TD-MLDFT procedure, the electronic excitations of the active part only are obtained as influenced by the presence of the inactive and MM layers.

4 Numerical Applications

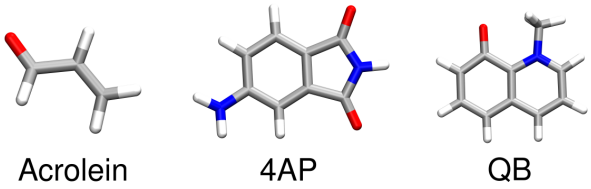

Figure 1: Molecular structures of Acrolein (left), 4-aminophthalimide (4AP, middle), and quinolinium betaine (QB, right).

To validate our novel approach, we apply it to the simulation of the absorption spectra of various organic systems dissolved in solution: acrolein, 4-aminophthalimide (4AP), and quinolinium betaine (QB). The molecular structures of the investigated systems are graphically depicted in Fig. 1. These systems are characterized by increasing electronic complexity, and their electronic transitions are highly affected by solvent effects.

4.1 Acrolein in aqueous solution

To first validate our approach, we consider the case of acrolein dissolved in aqueous solution. Besides its rather small size, the correct reproduction of acrolein vacuo-to-water solvatochromic shifts is particularly challenging.[12,74–81] Indeed, it has been reported that a proper description of solute-solvent electrostatics, polarization, and Pauli repulsion effects is crucial.[75] Thus, acrolein in water is ideal for validating our novel TD-MLDFT/FQ approach, which can, in principle, model all these interactions. In particular, we focus on the opposite vacuo-to-water solvatochromic shifts exhibited by the first electronic transitions, i.e. $n-\pi^*$ and $\pi-\pi^*$. The solute-solvent phase space is sampled by means of classical molecular dynamics (MD) by following the procedure reported in Ref. 12. In particular, the MD simulation is performed using GROMACS[82] exploiting OPLS-AA[83] force field to describe both intra- and

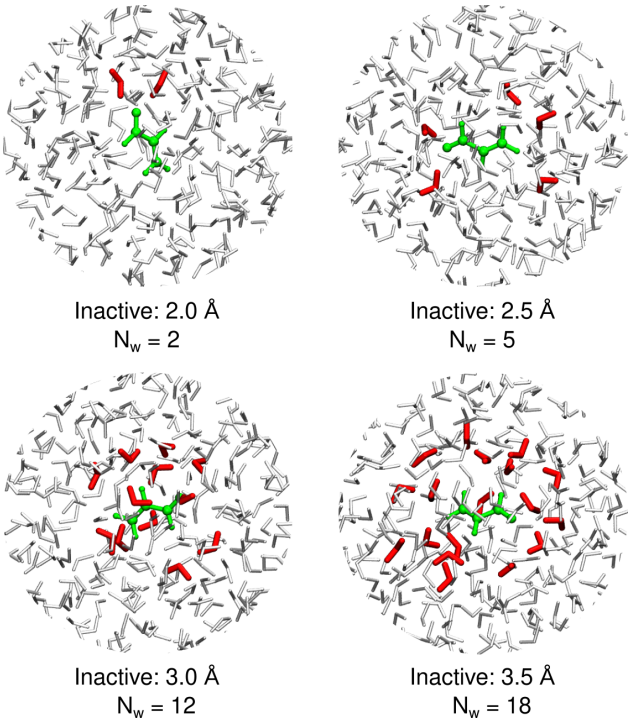

Figure 2: Graphical representation of MLDFT/FQ partitioning for acrolein in aqueous solution. Green: acrolein (active); red: inactive water molecules; silver: FQ water molecules. The radius of the inactive layer (from 2.0 to 3.5 Å) is reported together with the average number of inactive water molecules (N_w).

inter-molecular interactions. The TIP3P force field is used to describe water molecules.[84] ChelpG[85] scheme is employed to fit acrolein atomic charges for electrostatic interactions, while Van der Waals contributions are treated by relying on the parameterization proposed by Georg et al.[86] An NPT simulation for 1 ns is performed to obtain uniform distribution, followed by a 10 ns production run in the NVT ensemble (acrolein is free to move). The MD analysis and further computational details can be found in Ref. 12

From the last 10 ns of the MD, 100 uncorrelated snapshots are extracted, and a sphere of radius 15 Å, centered on the solute, is cut.[12] The convergence of the computed spectra as a function of the snapshots is reported in Fig. S1 of the SI. The three-layer MLDFT/FQ and MLDFT$_{\mathrm{FQ}}$/FQ approaches are then used to calculate the excitation energies of solvated acrolein, which is treated as active. Thanks to its relatively small size, we also use acrolein as a test case to study how the dimension of the inactive shell affects the computed excitation energies. To this end, we include in the inactive region all water molecules that are placed at 2.0, 2.5, 3.0, and 3.5 Å from each solute atom. This automatically results in an increasing average number of water molecules (N_w) treated as inactive at the DFT level (see Fig. 2). Both the active and inactive regions are treated at the B3LYP/aug-cc-pVDZ level of theory. The remaining water molecules are instead described by means of the FQ force field by using the parametrization reported in Ref. 87. To analyze whether MLDFT($_{\mathrm{FQ}}$)/FQ can account for the largest part of active-inactive polarization effects in the GS, acrolein excitation energies in aqueous solution are also computed by fully incorporating such effects. This is done by performing a GS DFT/FQ calculation including in the QM region all atoms defining the MLDFT portion (i.e. all molecules within this region are treated as active). This is followed by a Cholesky decomposition (Eq. 16) of the SCF converged density matrix of the full system. The obtained MOs are used to construct the active (and inactive) density matrices and exploited to define the active reduced MO space in TDDFT response equations. In the response calculations, the inactive layer is endowed with FQ charges as in MLDFT$_{\mathrm{FQ}}$/FQ method. We name this approach MLDFT$_{\mathrm{FQ}}$-in-DFT/FQ.

Table 1: Calculated vertical excitation energies for $n-\pi^*$ and $\pi-\pi^*$ transitions of acrolein in vacuo and aqueous solution obtained at the QM/FQ, MLDFT/FQ, MLDFT_{FQ}/FQ, and MLDFT_{FQ}-in-DFT/FQ levels. MLDFT($_{\text{FQ}}$)/FQ and MLDFT_{FQ}-in-DFT/FQ results are given as a function of the inactive radius (from 2.0 to 3.5 Å). Vacuo-to-water solvatochromic shifts are also provided in parenthesis. The experimental values are recovered from Ref. 74.

Radius	Method.	$E_{n-\pi^*}$ (eV)	$E_{\pi-\pi^*}$ (eV)
	vacuo	3.56	6.17
	Exp.(vacuo)	3.69	6.42
	QM/FQ	4.00 (-0.44)	5.71 (0.46)
2.0Å	MLDFT/FQ	3.94 (-0.38)	5.75 (0.42)
	MLDFT_{FQ}/FQ	3.93 (-0.37)	5.71 (0.46)
	MLDFT_{FQ}-in-DFT/FQ	3.94 (-0.38)	5.72 (0.45)
2.5Å	MLDFT/FQ	3.94 (-0.38)	5.79 (0.38)
	MLDFT_{FQ}/FQ	3.94 (-0.38)	5.74 (0.43)
	MLDFT_{FQ}-in-DFT/FQ	3.96 (-0.40)	5.74 (0.43)
3.0Å	MLDFT/FQ	3.94 (-0.38)	5.78 (0.39)
	MLDFT_{FQ}/FQ	3.93 (-0.37)	5.68 (0.49)
	MLDFT_{FQ}-in-DFT/FQ	3.96 (-0.40)	5.68 (0.49)
3.5Å	MLDFT/FQ	3.95 (-0.39)	5.80 (0.37)
	MLDFT_{FQ}/FQ	3.95 (-0.39)	5.69 (0.48)
	MLDFT_{FQ}-in-DFT/FQ	3.97 (-0.41)	5.69 (0.48)
	Exp.(water)	3.94 (-0.25)	5.90 (0.52)

The electronic excitation energies calculated at the MLDFT/FQ, MLDFT$_{\mathrm{FQ}}$/FQ, and MLDFT$_{\mathrm{FQ}}$-in-DFT/FQ levels as a function of the inactive radius are reported in Tab. 1. Let us first focus on the dark $n-\pi^*$ electronic transition (see Fig. S2 in the SI). The vertical excitation energies computed by the three approaches provide almost the same excitation energy independently of the considered inactive radius, with the largest discrepancy reported for $r = 3.0$Å. However, also in this case, the difference between the three approaches is below the chemical accuracy (~ 0.04 eV). The almost perfect agreement between the fully polarized (in the GS) MLDFT$_{\mathrm{FQ}}$-in-DFT/FQ and the other methods show that the latter are able to account for the largest part of GS polarization active-inactive polarization effects. In addition, we note that the almost equal description provided by MLDFT/FQ and MLDFT$_{\mathrm{FQ}}$/FQ methods is due to the nature of the $n-\pi^*$ excitation. In this case, the solvent dynamic polarization introduced in MLDFT$_{\mathrm{FQ}}$/FQ in the linear response formalism is negligible since the transition is dark (transition dipole moment ~ 0). This is in agreement with previous studies that exploit different solvent models.[79,88] We also note that the computed $n-\pi^*$ excitation energy values rapidly reach convergence as a function of the inactive radius since only slight variations are reported for radii larger than 2.0 Å.

A different outcome is obtained for $\pi-\pi^*$ transition energies (see Tab. 1 and Fig. S2 in the SI). In fact, the inclusion of polarization effects in the linear response (MLDFT$_{\mathrm{FQ}}$/FQ vs. MLDFT/FQ) yields a general decrease in the excitation energies. Such decrease becomes more significant as the inactive radius is increased from 2.0 Å to 3.5 Å. This is particularly evident for the largest radii (3.0 Å and 3.5 Å), for which polarization effects shift MLDFT/FQ results of 0.09 and 0.12 eV, respectively. A substantial response polarization effect is expected for $\pi-\pi^*$ excitations due to the associated large transition dipole moment. The obtained shifts are in agreement with previous data reported in the literature for other polarizable classical embedding approaches,[74,75,88] demonstrating the robustness of our developed approach. Furthermore, MLDFT$_{\mathrm{FQ}}$/FQ data are perfectly in agreement with the reference MLDFT$_{\mathrm{FQ}}$-in-DFT/FQ, with the largest discrepancy (0.01 eV) reported for

the smallest inactive radius (2.0 Å). This again demonstrates that GS polarization effects are considered in MLDFT$_{\mathrm{FQ}}$/FQ approach, and that the commented differences with respect to MLDFT/FQ can be ascribed to the inclusion of polarization effects in the response equations.

To better highlight the effect of the inactive layer, our results can be compared with the QM/FQ method, in which both the ground and linear response calculations are calculated at the QM/FQ level, including acrolein only in the QM region. Within QM/FQ, solute-solvent interactions are classically described and are thus limited to electrostatics and polarization. Differently, in MLDFT$_{\mathrm{FQ}}$/FQ, the solute-solvent interactions include electrostatics, polarization, and Pauli repulsion effects, which act as a quantum confinement of the solute density. Consequently, the difference between MLDFT$_{\mathrm{FQ}}$/FQ and QM/FQ results is primarily related to solute-solvent Pauli repulsion effects and, secondly, to the refined electrostatic (and polarization) descriptions provided by MLDFT$_{\mathrm{FQ}}$/FQ. As it can be appreciated from the results reported in Tab. 1, MLDFT$_{\mathrm{FQ}}$/FQ $n-\pi^*$ excitation energies are systematically higher than QM/FQ ones, while the opposite holds for $\pi-\pi^*$ transition (for inactive radii $\geq$ 3.0 Å). Such a finding agrees with what has been reported previously by some of us exploiting a QM/MM treatment of Pauli repulsion effects.[12]

To better analyze our results and quantify solvent effects on electronic transitions, the vacuo-to-water solvatochromic shift is also evaluated as the difference between the calculated excitation energies in vacuo and water. Acrolein gas-phase geometry is optimized at the B2PLYP/cc-pVTZ level in agreement with Ref. 75, while vertical excitations are obtained at the B3LYP/aug-cc-pVDZ level. Computed solvatochromic shifts are compared with experimental data reported in Ref. 74. The computed DFT energies for both $n-\pi^*$ and $\pi-\pi^*$ transitions are shifted with respect to the experimental reference. This is associated with the well-known systematic error of DFT functionals. However, this error can be substantially reduced by comparing computed and experimental energy differences, such as solvatochromic shifts.[89] The latter are given in brackets in Tab. 1. We first note that the

inclusion of solvent effects has an opposite trend for the two studied transitions, yielding to a red- or blueshift for $n-\pi^*$ and $\pi-\pi^*$ excitations, respectively. All computed solvatochromic shifts for $n-\pi^*$ excitation deviate from the experimental reference. This can be ascribed to the fact that a linear response formalism cannot account for a proper description of state-specific electronic solvent relaxation, which is required to accurately describe solvent effects on $n-\pi^*$ excitations.[12,88] However, it is worth remarking that the introduction of confinement effects in MLDFT($_{\text{FQ}}$)/FQ shifts the computed results towards the experimental reference as compared to QM/FQ, thus reducing the computed error. By moving to $\pi-\pi^*$, the MLDFT$_{\text{FQ}}$/FQ computed results show a notable agreement with the experimental solvatochromic shift, especially for the largest inactive radii. In particular, including response polarization effects (MLDFT$_{\text{FQ}}$/FQ vs. MLDFT/FQ) is crucial to obtain an almost perfect agreement with the reference. This demonstrates the robustness of our modeling of such effects. Confinement effects, which can be estimated by comparing MLDFT$_{\text{FQ}}$/FQ and QM/FQ results, instead play a minor role compared to response polarization effects. However, for inactive regions larger than 3 Å, they shift the computed solvatochromic shift towards the experiment, reducing QM/FQ error to just 0.04 (3.0 Å) and 0.03 (3.5 Å) eV.

4.2 4-aminophtalimide in aqueous solution

To further test our novel MLDFT($_{\text{FQ}}$)/FQ approach, we apply it to simulate the electronic excitations of 4-Aminophthalimide (4AP) dissolved in aqueous solution. Also in this case, MLDFT($_{\text{FQ}}$)/FQ is compared to QM/FQ by calculating the UV-Vis spectrum on 50 uncorrelated snapshots extracted from a classical MD simulation. The MD simulation is performed according to Ref. 90, by using GROMACS,[82] with the GAFF[91,92] force field to describe intra- and inter-molecular interactions and CM5 charges for electrostatic interactions. The TIP3P-FB force field is used to describe the water molecules.[93] To obtain a uniform distribution, an NPT simulation is performed, followed by a 100 ns production run in the NVT ensemble, with 4AP free to move. The MD analysis and further computational details are

given in Ref. 90.

Each snapshot is cut in a spherical shape with a radius equal to 17 Å. The convergence of the computed spectrum as a function of the number of snapshots is reported in Fig. S3 in the SI. In MLDFT($_{\mathrm{FQ}}$)/FQ calculations, 4AP is treated as active at the B3LYP/aug-cc-pVDZ level. The water molecules within 3.5 Å from each 4AP atom are included in the inactive layer and are treated at the B3LYP/cc-pVDZ level. All the remaining waters are described by means of the FQ force field exploiting the parametrization reported in Ref. 87.

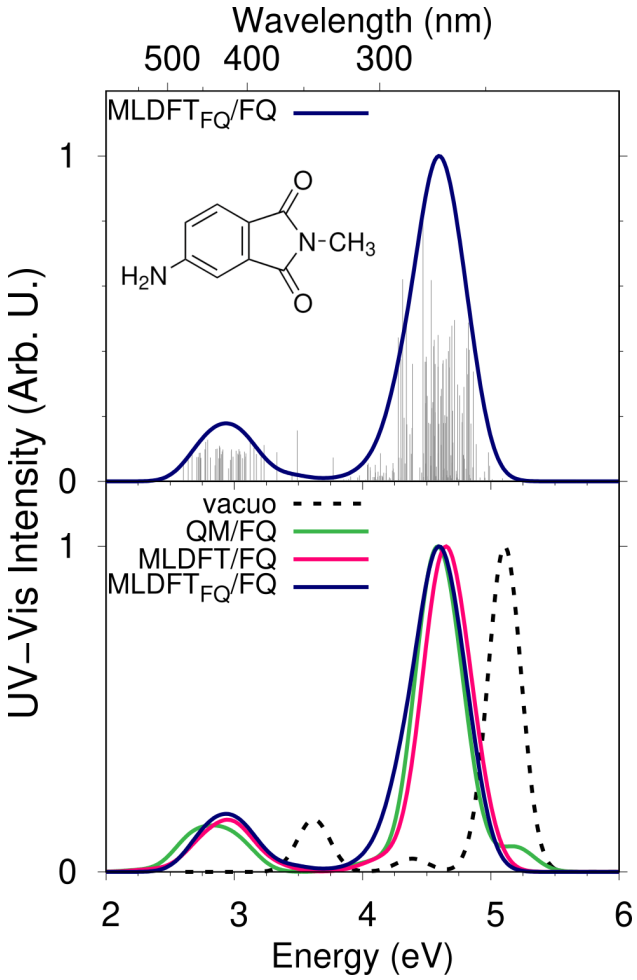

Figure 3: (top) MLDFT$_{\mathrm{FQ}}$/FQ absorption stick spectrum of 4AP in aqueous solution, and its Gaussian convolution (FWHM = 0.3 eV). (bottom) Computed QM/FQ, MLDFT/FQ and MLDFT$_{\mathrm{FQ}}$/FQ absorption spectra of 4AP in aqueous solution together with the gas-phase absorption spectrum.

Figure 3 reports the computed spectra in the gas phase and in solution obtained using

QM/FQ, MLDFT/FQ, and MLDFT$_{\mathrm{FQ}}$/FQ. In all cases, the first six excited states are considered in the TDDFT response. In the upper panel, the MLDFT$_{\mathrm{FQ}}$/FQ raw data extracted from each snapshot are graphically depicted as stick spectra, together with their Gaussian convolution (FWHM = 0.3 eV). A large variability in both excitation energies and intensities as a function of the snapshot is reported. This results from the coupling between fully atomistic techniques, such as QM/FQ and MLDFT$_{\mathrm{FQ}}$/FQ, with the dynamical sampling of the solute-solvent phase-space provided by the classical MD simulation. When convoluted, this variability translates into inhomogeneous band broadening, which is thus automatically included within our methodology.

The lower panel highlights the crucial role of solvent effects by comparing embedding methods with the vacuo result. 4AP gas-phase geometry and the first six excitation energies are calculated at the B3LYP/aug-cc-pVDZ level. The gas-phase spectrum is dominated by two main peaks at about 3.6 and 5.2 eV. A similar outcome is obtained for the computed spectra in solution, for which a significant redshift in the peaks is reported. This result highlights the relevance of solvent effects for 4AP in aqueous solution. This is not unexpected and can be related to 4AP molecular structure. In fact, its nitrogen and oxygen atoms can strongly interact with water molecules *via* hydrogen bonding. Furthermore, its diffuse π-electron cloud suggests that other interactions might also play a significant role. These effects can be analyzed by comparing the selected embedding models. By focusing on the first electronic transition (at about 3 eV), the inclusion of Pauli repulsion effects in MLDFT($_{\mathrm{FQ}}$)/FQ blueshifts the peak of about 0.15 eV as compared to the purely electrostatic polarizable QM/FQ band. For this peak, associated with a HOMO-LUMO transition with $n-\pi^*$ character (see Fig. S4 in the SI), MLDFT$_{\mathrm{FQ}}$/FQ and MLDFT/FQ methods provide very similar excitation energy, with a slight discrepancy in the intensities. By considering the main band of the spectrum at about 4.6 eV, we observe that QM/FQ and MLDFT$_{\mathrm{FQ}}$/FQ yield the same excitation energies (4.59 eV). In comparison, a redshift of about 0.07 eV is reported for MLDFT/FQ, remarking the relevant of polarization effects in response equations. This band

results from the convolution of several transitions, all characterized by a $\pi - \pi^*$ character (see Fig. S4 and Tab. S1 in the SI). Therefore, the results obtained for 4AP perfectly agree with those reported for acrolein, highlighting the diverse physicochemical contributions of solute-solvent interaction terms on electronic transitions.

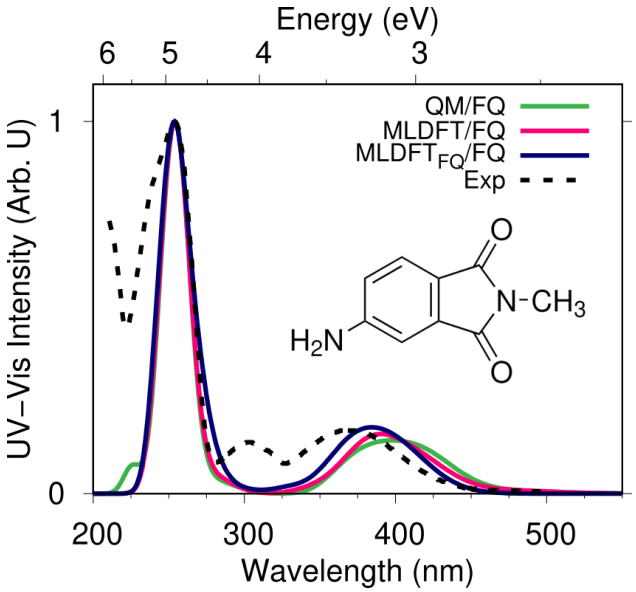

Figure 4: Calculated absorption spectra of 4AP in aqueous solution obtained at the QM/FQ, MLDFT/FQ, and MLDFT$_{FQ}$/FQ levels. The experimental spectrum, reproduced from Ref. 94, is also graphically depicted. All calculated spectra are shifted to match the main experimental band at about 250 nm.

We now compare our results with the experimental spectrum of 4AP in aqueous solution. The experiment, reproduced from Ref. 94, is reported in Fig. 4 together with QM/FQ, MLDFT/FQ, and MLDFT$_{FQ}$/FQ computed spectra. Note that the computed spectra are shifted to match the main band of the experiment. The computed absolute excitation energies are, in fact, affected by DFT systematic errors. The experimental spectrum is characterized by two main peaks at about 250 and 370 nm. All embedding approaches reproduce this feature of the experiment. However, MLDFT$_{FQ}$/FQ better reproduces the relative energies of the peaks and their relative intensity. In fact, both MLDFT/FQ and QM/FQ bands at about 400 nm are redshifted and lower in intensity than the experiment. This confirms the reliability and robustness of the MLDFT$_{FQ}$/FQ approach, which accurately considers

solute-solvent electrostatics, polarization, and Pauli repulsion effects. Finally, note that the experimental spectrum presents a small band at about 300 nm, which is not reproduced by any embedding approaches. This is consistent with previous results reported in the literature obtained at various levels of theory (ranging from QM/PCM to QM/FDE/FQ).[26,90] Thus, the reported discrepancy can probably be associated with the lack of vibronic effects in the modeling or the improper description of electron correlation provided by DFT, requiring highly correlated methods, such as coupled cluster theory.

4.3 Solvatochromism of Quinolinium Betaine

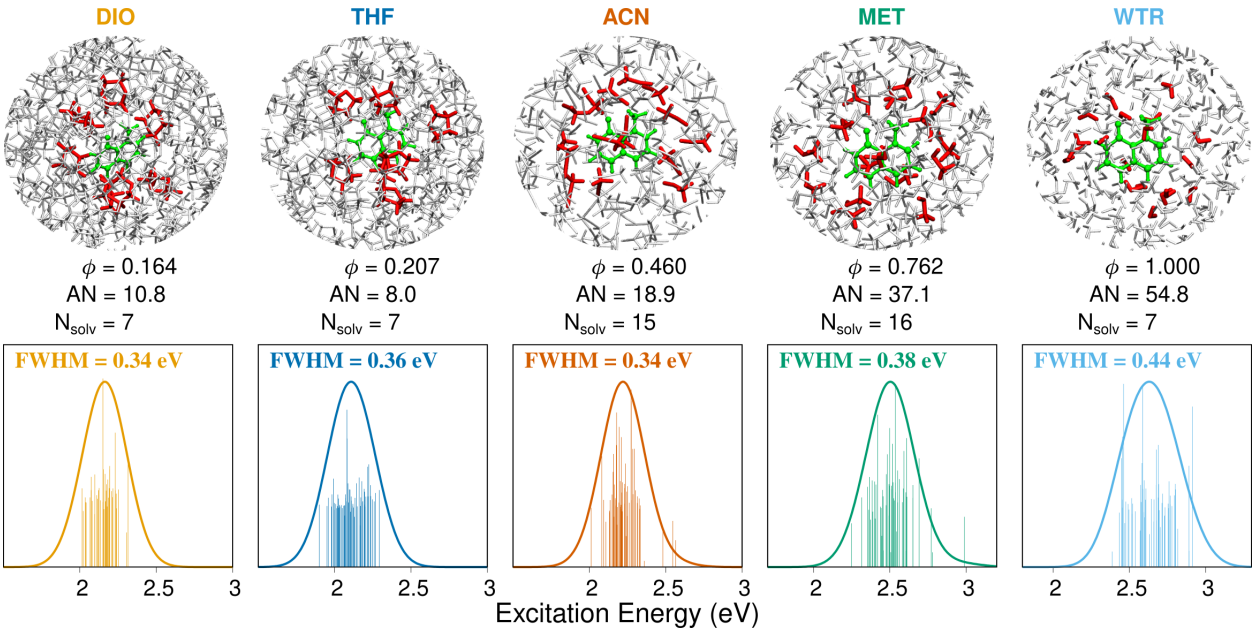

Figure 5: (top) Graphical representation of MLDFT/FQ partitioning for QB in the selected solvents (DIO, THF, ACN, MET and WTR). Green: QB (active); red: inactive solvent molecules; silver: FQ solvent molecules. For each solvent, the polarity parameters (ϕ and AN) are also provided, together with the average number of inactive solvent molecules. (bottom) MLDFT_{FQ}/FQ stick spectra of QB in the various solvents, alongside their Gaussian convolution (FWHM = 0.3 eV). The FWHM of the convoluted band is also given.

Quinolinium betaine (QB, see Fig. 1c) exhibits a zwitterionic character, making it highly hydrophilic. Its absorption spectrum is primarily governed by the transition from the dipolar GS to an ES with significantly reduced polarity. Consequently, the GS is highly stabilized in

polar solvents, thus manifesting positive solvatochromism due to increased transition energy as the solvent polarity increases. As a final test application, we investigate the solvatochromic shift of QB when dissolved in various solvents of increasing polarity, namely 1,4-dioxane (DIO), tetrahydrofuran (THF), acetonitrile (ACN), methanol (MET), and water (WTR). In this work, the polarity of the selected solvents is expressed in terms of the polarity scale proposed in Ref. 95 (Reichardt's normalized parameters - ϕ) and the acceptor number (AN) proposed in Ref. 96 (see Fig. 6, where a graphical representation of QB dissolved in the selected solvents is also provided). To describe solvent effects in the diverse solvents, we use QM/FQ and MLDFT$_{\mathrm{FQ}}$/FQ embedding methods. In particular, for each method and solvent, we focus on QB lowest bright excitation, which corresponds to the HOMO-LUMO transition with partial Charge Transfer character (see Fig. S5 in the SI). QM/FQ and MLDFT$_{\mathrm{FQ}}$/FQ excitation energies are calculated on 50 (DIO) and 60 (THF, ACN, MET, WTR) uncorrelated snapshots extracted from the last 2 ns of classical MD simulations performed according to Ref. 10 (the convergence of the computed spectra is reported in Fig. S6 in the SI). The MD is performed by using GROMACS,[82] with the GAFF force field for intra and intermolecular interactions,[91,92] RESP charges for electrostatic interactions[97] and the TIP3P force field for water molecules.[98] Considering QB rigid structure, the solute is constrained in its minimum energy structure during the MD run. An NPT simulation of 1 ns is performed for equilibrating the system. Then, a 2.5 ns NVT production run is performed. The MD analysis of the trajectory and further computational details are reported in Ref. 10.

For each solvent, the snapshots are cut in a spherical shape with a radius equal to 20 Å. In MLDFT$_{\mathrm{FQ}}$/FQ, the solvent molecules within 2.5 (DIO and THF) and 3.5 Å (ACN, MET, WTR) are included in the inactive portion, while QB is treated as active. All the remaining solvent molecules are described using the FQ force field and the parameters reported in Ref. 10. The average number of inactive solvent molecules ($\mathrm{N_{solv}}$) for each solvent is reported in Fig. 5, where a graphical description of each system is also provided.

In Fig. 5, the computed MLDFT$_{\mathrm{FQ}}$/FQ stick spectra and their Gaussian convolution (FWHM = 0.3 eV) are graphically depicted. For each solvent, a large variability in frequency and intensity is reported as a function of the snapshot. Such fluctuations increase as the polarity of the solvent increases. This can be analyzed by fitting the spectrum with a Gaussian function. The FWHM of the fitting Gaussian, which is a quantitative measure of band broadening, increases from 0.34 eV (DIO) to 0.44 eV (WTR). As expected, the nature of the solvent substantially affects the band broadening. Polar, protic solvents, such as MET and WTR, can establish hydrogen bonding interactions with QB, yielding to a larger spread in energies and intensities as compared to apolar, nonprotic solvents, such as DIO and THF. The calculated QM/FQ and MLDFT$_{\mathrm{FQ}}$/FQ excitation energies as a function of the solvent polarity (ϕ) are graphically depicted in Fig. 6a, together with their experimental counterparts from Ref. 99 (raw data are given in Tab. S2 in the SI). Both embedding approaches can effectively reproduce the experimental trend, which displays a huge positive solvatochromic shift as the polarity of the solvent increases. For $\phi < 0.5$, the QM/FQ excitation energies are in closer agreement with experimental values than MLDFT$_{\mathrm{FQ}}$/FQ. For the most polar solvents, QM/FQ excitation energies are instead larger than the experiments, while the opposite is valid for MLDFT$_{\mathrm{FQ}}$/FQ results. As commented above, the good agreement and the reported discrepancies can be attributed to systematic errors stemming from the chosen level of theory. Therefore, we now compare computed and experimental solvatochromic shifts, which are obtained as energy differences and are thus less susceptible to systematic errors.

In Fig. 6b, the solvatochromic shifts are computed with respect to excitation energies computed and measured for the lowest polar solvents since experimental QB gas-phase spectra are not reported in the literature (raw data are given in Tab. S3 in the SI). In particular, we report the solvatochromic shifts with respect to DIO (top) and THF (bottom), which are the lowest polar solvents in the ϕ and AN polarity scales, respectively. We first note that both QM/FQ and MLDFT$_{\mathrm{FQ}}$/FQ solvatochromic shifts in THF/DIO, i.e., the lowest

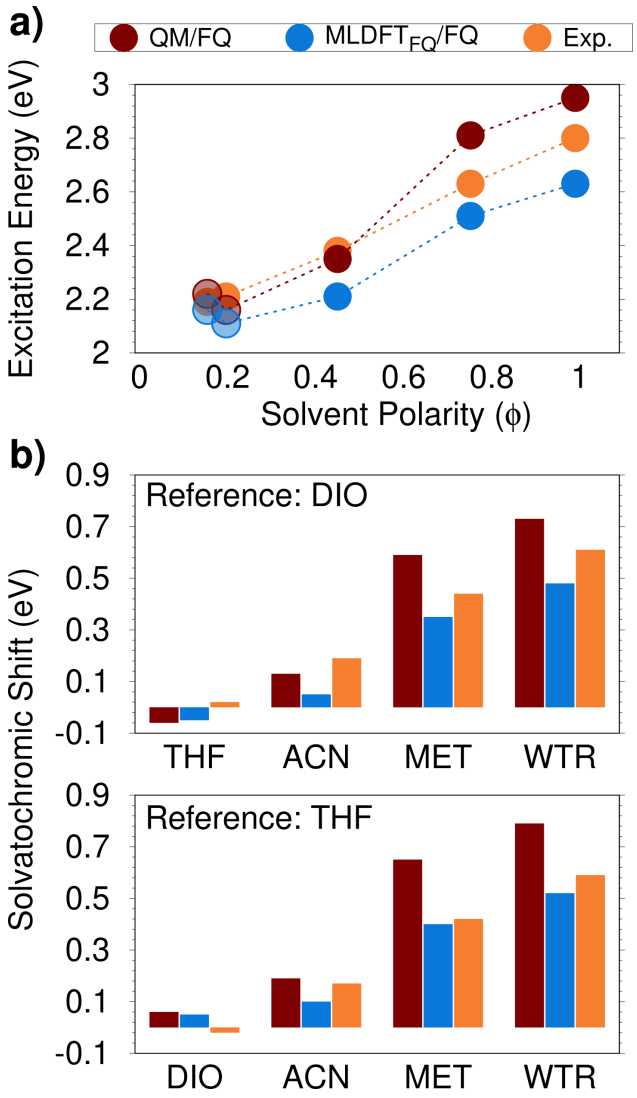

Figure 6: a) QM/FQ and MLDFT$_{FQ}$/FQ QB excitation energies as a function of the solvent polarity ϕ ; (b) QM/FQ and MLDFT$_{FQ}$/FQ solvatochromic shifts calculated by taking DIO (top) or THF (bottom) excitation energies as a reference. The experimental values are reproduced from Ref. 99.

polar solvents in the two scales, are incorrectly predicted in terms of the sign. However, the QM/FQ error can be considered acceptable, being approximately 0.08 eV ($\sim$ 1.86 kcal/mol) in both reference scales, which is reduced by 0.01 eV by using MLDFT$_{\mathrm{FQ}}$/FQ. Indeed, we note that QM/FQ shifts are systematically larger than the experimental counterpart, in particular for the most polar solvents (MET and WTR), and by taking THF as a reference. Indeed, the inclusion of solute-solvent quantum interactions, such as Pauli repulsion, decreases the computed shifts, bringing them towards the experiment, especially for MET and WTR. This demonstrates the crucial role of quantum interactions and the reliability of our novel MLDFT$_{\mathrm{FQ}}$/FQ, which can provide an almost perfect agreement with the experiments.

5 Summary and Conclusions

In this paper, we have introduced a novel three-layer approach based on multilevel density functional theory to simulate the electronic excitations of chemical systems embedded in an external environment. Our method is defined within the framework of quantum embedding approaches, where the electronic structure of the target system is determined in the field of an embedding inactive layer treated as frozen. To cost-effectively describe large systems, the immediate surroundings are described at the QM level, while long-range interactions are accounted for by employing the polarizable fluctuating charges force field. The resulting MLDFT/FQ approach thus accurately describes both electrostatics (and polarization) and non-electrostatic interactions. The method is extended to the time-dependent DFT formalism to describe electronic excitations of the target system. A notable feature of our model is its capability to consider the environment response of the inactive part by exploiting the classical FQ force field in the response equations. Consequently, the ground state electronic structure is evaluated at the MLDFT/FQ level, while the response equations are solved by modeling the entire environment (inactive layer+FQ) at the FQ level. This approach enables us to consider the full polarization effects of the environment without including the inactive

layer in the response equations, which would substantially increase computational costs. At the same time, our methodology retains MLDFT advantages for the ground state, such as active-inactive non-electrostatic effects, which are of purely quantum origin and are thus neglected in QM/classical approaches.

The developed MLDFT/FQ method has been validated by simulating the electronic absorption spectra of organic molecules in solution, which are characterized by increasing complexity. Our results demonstrate that our novel approach can effectively reproduce the experimental spectra and the measured solvatochromic effects, making it valuable for systems where non-electrostatic effects, typically disregarded in QM/classical calculations, play a significant role. To conclude, the developed approach is particularly versatile and has the potential to be applied to more complex systems. Specifically, it may be applied to systems where non-electrostatic interactions are expected to play a major role, for instance, adsorbed moieties on nanostructured plasmonic materials.

Acknowledgments

We gratefully acknowledge the Center for High-Performance Computing (CHPC) at SNS for providing the computational infrastructure. This work has received funding from the European Research Council (ERC) under the European Union's Horizon 2020 Research and Innovation Programme (Grant Agreement No. 101020016).

Supporting Information

Convergence of the computed spectra. MOs involved in the electronic transitions. Raw data of Fig. 6.

References

(1) Giovannini, T.; Egidi, F.; Cappelli, C. Molecular spectroscopy of aqueous solutions: a theoretical perspective. *Chem. Soc. Rev.* **2020**, *49*, 5664–5677.

(2) Mennucci, B.; Corni, S. Multiscale modelling of photoinduced processes in composite systems. *Nat. Rev. Chem.* **2019**, *3*, 315–330.

(3) Senn, H. M.; Thiel, W. QM/MM methods for biomolecular systems. *Angew. Chem. Int. Ed.* **2009**, *48*, 1198–1229.

(4) Tomasi, J.; Mennucci, B.; Cammi, R. Quantum mechanical continuum solvation models. *Chem. Rev.* **2005**, *105*, 2999–3094.

(5) Gordon, M. S.; Fedorov, D. G.; Pruitt, S. R.; Slipchenko, L. V. Fragmentation methods: A route to accurate calculations on large systems. *Chem. Rev.* **2012**, *112*, 632–672.

(6) Collins, M. A.; Cvitkovic, M. W.; Bettens, R. P. The combined fragmentation and systematic molecular fragmentation methods. *Acc. Chem. Res.* **2014**, *47*, 2776–2785.

(7) Collins, M. A.; Bettens, R. P. Energy-based molecular fragmentation methods. *Chem. Rev.* **2015**, *115*, 5607–5642.

(8) Warshel, A.; Levitt, M. Theoretical studies of enzymic reactions: dielectric, electrostatic and steric stabilization of the carbonium ion in the reaction of lysozyme. *J. Mol. Biol.* **1976**, *103*, 227–249.

(9) Giovannini, T.; Cappelli, C. Continuum vs. atomistic approaches to computational spectroscopy of solvated systems. *Chem. Commun.* **2023**, *59*, 5644–5660.

(10) Ambrosetti, M.; Skoko, S.; Giovannini, T.; Cappelli, C. Quantum Mechanics/Fluctuating Charge Protocol to Compute Solvatochromic Shifts. *J. Chem. Theory Comput.* **2021**, *17*, 7146–7156.

(11) Giovannini, T.; Lafiosca, P.; Cappelli, C. A General Route to Include Pauli Repulsion and Quantum Dispersion Effects in QM/MM Approaches. *J. Chem. Theory Comput.* **2017**, *13*, 4854–4870.

(12) Giovannini, T.; Ambrosetti, M.; Cappelli, C. Quantum Confinement Effects on Solvatochromic Shifts of Molecular Solutes. *J. Phys. Chem. Lett.* **2019**, *10*, 5823–5829.

(13) Reinholdt, P.; Kongsted, J.; Olsen, J. M. H. Polarizable Density Embedding: A Solution to the Electron Spill-Out Problem in Multiscale Modeling. *J. Phys. Chem. Lett.* **2017**, *8*, 5949–5958.

(14) Gordon, M. S.; Smith, Q. A.; Xu, P.; Slipchenko, L. V. Accurate first principles model potentials for intermolecular interactions. *Annu. Rev. Phys. Chem.* **2013**, *64*, 553–578.

(15) Sun, Q.; Chan, G. K.-L. Quantum embedding theories. *Acc. Chem. Res.* **2016**, *49*, 2705–2712.

(16) Knizia, G.; Chan, G. K.-L. Density matrix embedding: A strong-coupling quantum embedding theory. *J. Chem. Theory. Comput.* **2013**, *9*, 1428–1432.

(17) Goodpaster, J. D.; Barnes, T. A.; Manby, F. R.; Miller III, T. F. Density functional theory embedding for correlated wavefunctions: Improved methods for open-shell systems and transition metal complexes. *J. Chem. Phys.* **2012**, *137*, 224113.

(18) Manby, F. R.; Stella, M.; Goodpaster, J. D.; Miller III, T. F. A simple, exact density-functional-theory embedding scheme. *J. Chem. Theory Comput.* **2012**, *8*, 2564–2568.

(19) Zhang, K.; Ren, S.; Caricato, M. Multi-state QM/QM Extrapolation of UV/Vis Absorption Spectra with Point Charge Embedding. *J. Chem. Theory Comput.* **2020**, *16*, 4361–4372.

(20) Ramos, P.; Papadakis, M.; Pavanello, M. Performance of frozen density embedding for modeling hole transfer reactions. *J. Phys. Chem. B* **2015**, *119*, 7541–7557.

(21) Pavanello, M.; Neugebauer, J. Modelling charge transfer reactions with the frozen density embedding formalism. *J. Chem. Phys.* **2011**, *135*, 234103.

(22) Tamukong, P. K.; Khait, Y. G.; Hoffmann, M. R. Density differences in embedding theory with external orbital orthogonality. *The Journal of Physical Chemistry A* **2014**, *118*, 9182–9200.

(23) Tamukong, P. K.; Khait, Y. G.; Hoffmann, M. R. Accurate dissociation of chemical bonds using DFT-in-DFT embedding theory with external orbital orthogonality. *J. Phys. Chem. A* **2017**, *121*, 256–264.

(24) Wesolowski, T. A. Hydrogen-bonding-induced shifts of the excitation energies in nucleic acid bases: an interplay between electrostatic and electron density overlap effects. *J. Am. Chem. Soc.* **2004**, *126*, 11444–11445.

(25) Neugebauer, J.; Louwerse, M. J.; Belanzoni, P.; Wesolowski, T. A.; Baerends, E. J. Modeling solvent effects on electron-spin-resonance hyperfine couplings by frozen-density embedding. *J. Chem. Phys.* **2005**, *123*, 114101.

(26) Egidi, F.; Angelico, S.; Lafiosca, P.; Giovannini, T.; Cappelli, C. A polarizable three-layer frozen density embedding/molecular mechanics approach. *J. Chem. Phys.* **2021**, *154*.

(27) Neugebauer, J.; Louwerse, M. J.; Baerends, E. J.; Wesolowski, T. A. The merits of the frozen-density embedding scheme to model solvatochromic shifts. *J. Chem. Phys.* **2005**, *122*, 094115.

(28) Wesolowski, T. A.; Shedge, S.; Zhou, X. Frozen-density embedding strategy for multilevel simulations of electronic structure. *Chem. Rev.* **2015**, *115*, 5891–5928.

(29) Fux, S.; Jacob, C. R.; Neugebauer, J.; Visscher, L.; Reiher, M. Accurate frozen-density embedding potentials as a first step towards a subsystem description of covalent bonds. *J. Chem. Phys.* **2010**, *132*, 164101.

(30) Jacob, C. R.; Neugebauer, J.; Visscher, L. A flexible implementation of frozen-density embedding for use in multilevel simulations. *J. Comput. Chem.* **2008**, *29*, 1011–1018.

(31) Jacob, C. R.; Visscher, L. Calculation of nuclear magnetic resonance shieldings using frozen-density embedding. *J. Chem. Phys.* **2006**, *125*, 194104.

(32) Jacob, C. R.; Neugebauer, J.; Jensen, L.; Visscher, L. Comparison of frozen-density embedding and discrete reaction field solvent models for molecular properties. *Phys. Chem. Chem. Phys.* **2006**, *8*, 2349–2359.

(33) Wesołowski, T. A. Embedding a multideterminantal wave function in an orbital-free environment. *Phys. Rev. A* **2008**, *77*, 012504.

(34) Bennie, S. J.; Curchod, B. F.; Manby, F. R.; Glowacki, D. R. Pushing the limits of EOM-CCSD with projector-based embedding for excitation energies. *J. Phys. Chem. Lett.* **2017**, *8*, 5559–5565.

(35) Chulhai, D. V.; Goodpaster, J. D. Projection-based correlated wave function in density functional theory embedding for periodic systems. *J. Chem. Theory Comput.* **2018**, *14*, 1928–1942.

(36) Marrazzini, G.; Giovannini, T.; Scavino, M.; Egidi, F.; Cappelli, C.; Koch, H. Multilevel density functional theory. *J. Chem. Theory Comput.* **2021**, *17*, 791–803.

(37) Giovannini, T.; Marrazzini, G.; Scavino, M.; Koch, H.; Cappelli, C. Integrated Multiscale Multilevel Approach to Open Shell Molecular Systems. *J. Chem. Theory Comput.* **2023**, *19*, 1446–1456.

(38) Wesolowski, T. A.; Warshel, A. Frozen density functional approach for ab initio calculations of solvated molecules. *J. Phys. Chem.* **1993**, *97*, 8050–8053.

(39) Sæther, S.; Kjærgaard, T.; Koch, H.; Høyvik, I.-M. Density-Based Multilevel Hartree–Fock Model. *J. Chem. Theory Comput.* **2017**, *13*, 5282–5290.

(40) Høyvik, I.-M. Convergence acceleration for the multilevel Hartree–Fock model. *Mol. Phys.* **2020**, *118*, 1626929.

(41) Goletto, L.; Kjønstad, E. F.; Folkestad, S. D.; Høyvik, I.-M.; Koch, H. Linear-Scaling Implementation of Multilevel Hartree–Fock Theory. *J. Chem. Theory Comput.* **2021**, *17*, 7416–7427.

(42) Goletto, L.; Gómez, S.; Andersen, J. H.; Koch, H.; Giovannini, T. Linear response properties of solvated systems: a computational study. *Phys. Chem. Chem. Phys.* **2022**, *24*, 27866–27878.

(43) Casida, M. E. In *Recent Advances in Density Functional Methods Part I*; Chong, D. P., Ed.; World Scientific, Singapore, 1995; pp 155–192.

(44) Cappelli, C. Integrated QM/Polarizable MM/Continuum Approaches to Model Chiroptical Properties of Strongly Interacting Solute-Solvent Systems. *Int. J. Quantum Chem.* **2016**, *116*, 1532–1542.

(45) Rick, S. W.; Stuart, S. J.; Berne, B. J. Dynamical fluctuating charge force fields: Application to liquid water. *J. Chem. Phys.* **1994**, *101*, 6141–6156.

(46) Myhre, R. H.; Koch, H. The multilevel CC3 coupled cluster model. *J. Chem. Phys.* **2016**, *145*, 044111.

(47) Myhre, R. H.; Sánchez de Merás, A. M.; Koch, H. Multi-level coupled cluster theory. *J. Chem. Phys.* **2014**, *141*, 224105.

(48) Folkestad, S. D.; Koch, H. Equation-of-motion MLCCSD and CCSD-in-HF oscillator strengths and their application to core excitations. *J. Chem. Theory Comput.* **2020**, *16*, 6869–6879.

(49) Giovannini, T.; Koch, H. Energy-Based Molecular Orbital Localization in a Specific Spatial Region. *J. Chem. Theory Comput.* **2021**, *17*, 139–150.

(50) Sánchez de Merás, A. M.; Koch, H.; Cuesta, I. G.; Boman, L. Cholesky decomposition-based definition of atomic subsystems in electronic structure calculations. *J. Chem. Phys.* **2010**, *132*, 204105.

(51) Olsen, J. M.; Aidas, K.; Kongsted, J. Excited states in solution through polarizable embedding. *J. Chem. Theory Comput.* **2010**, *6*, 3721–3734.

(52) Olsen, J. M. H.; Kongsted, J. Molecular properties through polarizable embedding. *Adv. Quantum Chem.* **2011**, *61*, 107–143.

(53) Olsen, J. M. H.; Steinmann, C.; Ruud, K.; Kongsted, J. Polarizable density embedding: A new QM/QM/MM-based computational strategy. *J. Phys. Chem. A* **2015**, *119*, 5344–5355.

(54) Rick, S. W.; Stuart, S. J.; Bader, J. S.; Berne, B. Fluctuating charge force fields for aqueous solutions. *J. Mol. Liq.* **1995**, *65*, 31–40.

(55) Rick, S. W.; Berne, B. J. Dynamical Fluctuating Charge Force Fields: The Aqueous Solvation of Amides. *J. Am. Chem. Soc.* **1996**, *118*, 672–679.

(56) Lipparini, F.; Cappelli, C.; Barone, V. Linear response theory and electronic transition energies for a fully polarizable QM/classical hamiltonian. *J. Chem. Theory Comput.* **2012**, *8*, 4153–4165.

(57) Gómez, S.; Giovannini, T.; Cappelli, C. Multiple facets of modeling electronic absorption spectra of systems in solution. *ACS Phys. Chem. Au* **2023**, *3*, 1–16.

(58) Casida, M. E.; Wesołowski, T. A. Generalization of the Kohn–Sham equations with constrained electron density formalism and its time-dependent response theory formulation. *Int. J. Quantum Chem.* **2004**, *96*, 577–588.

(59) Neugebauer, J. Couplings between electronic transitions in a subsystem formulation of time-dependent density functional theory. *J. Chem. Phys.* **2007**, *126*, 134116.

(60) Neugebauer, J. Photophysical properties of natural light-harvesting complexes studied by subsystem density functional theory. *J. Phys. Chem. B* **2008**, *112*, 2207–2217.

(61) Van den Heuvel, W.; Reinholdt, P.; Kongsted, J. Embedding Beyond Electrostatics: The Extended Polarizable Density Embedding Model. *J. Phys. Chem. B* **2023**, *127*, 3248–3256.

(62) Nåbo, L. J.; Olsen, J. M. H.; Holmgaard List, N.; Solanko, L. M.; Wüstner, D.; Kongsted, J. Embedding beyond electrostatics—The role of wave function confinement. *J. Chem. Phys.* **2016**, *145*, 104102.

(63) Folkestad, S. D.; Kjønstad, E. F.; Myhre, R. H.; Andersen, J. H.; Balbi, A.; Coriani, S.; Giovannini, T.; Goletto, L.; Haugland, T. S.; Hutcheson, A., et al. e T 1.0: An open source electronic structure program with emphasis on coupled cluster and multilevel methods. *J. Chem. Phys.* **2020**, *152*, 184103.

(64) Lebedev, V. I.; Laikov, D. *Doklady Mathematics*; 1999; Vol. 59; pp 477–481.

(65) Krack, M.; Köster, A. M. An adaptive numerical integrator for molecular integrals. *J. Chem. Phys.* **1998**, *108*, 3226–3234.

(66) Marques, M. A.; Oliveira, M. J.; Burnus, T. Libxc: A library of exchange and correlation functionals for density functional theory. *Comput. Phys. Commun.* **2012**, *183*, 2272–2281.

(67) Lehtola, S.; Steigemann, C.; Oliveira, M. J.; Marques, M. A. Recent developments in libxc—A comprehensive library of functionals for density functional theory. *SoftwareX* **2018**, *7*, 1–5.

(68) He, X.; Merz Jr, K. M. Divide and conquer Hartree- Fock calculations on proteins. *J. Chem. Theory Comput.* **2010**, *6*, 405–411.

(69) Aquilante, F.; Boman, L.; Boström, J.; Koch, H.; Lindh, R.; de Merás, A. S.; Pedersen, T. B. *Linear-Scaling Techniques in Computational Chemistry and Physics*; Springer, 2011; pp 301–343.

(70) Koch, H.; Sánchez de Merás, A.; Pedersen, T. B. Reduced scaling in electronic structure calculations using Cholesky decompositions. *J. Chem. Phys.* **2003**, *118*, 9481–9484.

(71) Christiansen, O.; Manninen, P.; Jørgensen, P.; Olsen, J. Coupled-cluster theory in a projected atomic orbital basis. *J. Chem. Phys.* **2006**, *124*, 084103.

(72) Høyvik, I.-M.; Kristensen, K.; Kjærgaard, T.; Jørgensen, P. *Thom H. Dunning, Jr.*; Springer, 2015; pp 287–296.

(73) Saebo, S.; Pulay, P. Local treatment of electron correlation. *Annu. Rev. Phys. Chem.* **1993**, *44*, 213–236.

(74) Aidas, K.; Møgelhøj, A.; Nilsson, E. J.; Johnson, M. S.; Mikkelsen, K. V.; Christiansen, O.; Söderhjelm, P.; Kongsted, J. On the performance of quantum chemical methods to predict solvatochromic effects: The case of acrolein in aqueous solution. *J. Chem. Phys.* **2008**, *128*, 194503.

(75) Goletto, L.; Giovannini, T.; Folkestad, S. D.; Koch, H. Combining multilevel Hartree–Fock and multilevel coupled cluster approaches with molecular mechanics: a study of electronic excitations in solutions. *Phys. Chem. Chem. Phys.* **2021**, *23*, 4413–4425.

(76) Moskvin, A.; Yablonskii, O.; Bondar, L. An experimental investigation of the effect of alkyl substituents on the position of the K and R absorption bands in acrolein derivatives. *Theor. Exp. Chem.* **1966**, *2*, 469–472.

(77) Aquilante, F.; Barone, V.; Roos, B. O. A theoretical investigation of valence and Rydberg electronic states of acrolein. *J. Chem. Phys.* **2003**, *119*, 12323–12334.

(78) Brancato, G.; Rega, N.; Barone, V. A quantum mechanical/molecular dynamics/mean field study of acrolein in aqueous solution: Analysis of H bonding and bulk effects on spectroscopic properties. *J. Chem. Phys.* **2006**, *125*, 164515.

(79) Marenich, A. V.; Cramer, C. J.; Truhlar, D. G.; Guido, C. A.; Mennucci, B.; Scalmani, G.; Frisch, M. J. Practical computation of electronic excitation in solution: vertical excitation model. *Chem. Sci.* **2011**, *2*, 2143–2161.

(80) Duchemin, I.; Guido, C. A.; Jacquemin, D.; Blase, X. The Bethe–Salpeter formalism with polarisable continuum embedding: reconciling linear-response and state-specific features. *Chem. Sci.* **2018**, *9*, 4430–4443.

(81) Bistafa, C.; Modesto-Costa, L.; Canuto, S. A complete basis set study of the lowest n–π^* and π–π^* electronic transitions of acrolein in explicit water environment. *Theor. Chem. Acc.* **2016**, *135*, 129.

(82) Abrahama, M. J.; Murtola, T.; Schulz, R.; Pálla, S.; Smith, J. C.; Hess, B.; Lindahl, E. GROMACS: High Performance Molecular Simulations through Multi-Level Parallelism from Laptops to Supercomputers. *SoftwareX* **2015**, *1-2*, 19–25.

(83) Jorgensen, W. L.; Maxwell, D. S.; Tirado-Rives, J. Development and testing of the OPLS all-atom force field on conformational energetics and properties of organic liquids. *J. Am. Chem. Soc.* **1996**, *118*, 11225–11236.

(84) Mark, P.; Nilsson, L. Structure and dynamics of the TIP3P, SPC, and SPC/E water models at 298 K. *J. Phys. Chem. A* **2001**, *105*, 9954–9960.

(85) Breneman, C. M.; Wiberg, K. B. Determining atom-centered monopoles from molecular electrostatic potentials. The need for high sampling density in formamide conformational analysis. *J. Comput. Chem.* **1990**, *11*, 361–373.

(86) Georg, H. C.; Coutinho, K.; Canuto, S. A sequential Monte Carlo quantum mechanics study of the hydrogen-bond interaction and the solvatochromic shift of the n–π^* transition of acrolein in water. *J. Chem. Phys.* **2005**, *123*, 124307.

(87) Giovannini, T.; Lafiosca, P.; Chandramouli, B.; Barone, V.; Cappelli, C. Effective yet Reliable Computation of Hyperfine Coupling Constants in Solution by a QM/MM Approach: Interplay Between Electrostatics and Non-electrostatic Effects. *J. Chem. Phys.* **2019**, *150*, 124102.

(88) Caricato, M.; Mennucci, B.; Tomasi, J.; Ingrosso, F.; Cammi, R.; Corni, S.; Scalmani, G. Formation and relaxation of excited states in solution: A new time dependent polarizable continuum model based on time dependent density functional theory. *J. Chem. Phys.* **2006**, *124*, 124520.

(89) Loco, D.; Polack, É.; Caprasecca, S.; Lagardere, L.; Lipparini, F.; Piquemal, J.-P.; Mennucci, B. A QM/MM approach using the AMOEBA polarizable embedding: from ground state energies to electronic excitations. *J. Chem. Theory Comput.* **2016**, *12*, 3654–3661.

(90) Giovannini, T.; Macchiagodena, M.; Ambrosetti, M.; Puglisi, A.; Lafiosca, P.; Lo Gerfo, G.; Egidi, F.; Cappelli, C. Simulating vertical excitation energies of solvated dyes: From continuum to polarizable discrete modeling. *Int. J. Quantum Chem.* **2019**, *119*, e25684.

(91) Wang, J.; Wolf, R. M.; Caldwell, J. W.; Kollman, P. A.; Case, D. A. Development and testing of a general amber force field. *J. Comput. Chem.* **2004**, *25*, 1157–1174.

(92) Wang, J.; Wang, W.; Kollman, P. A.; Case, D. A. Automatic atom type and bond type perception in molecular mechanical calculations. *J. Mol. Graph. Model.* **2006**, *25*, 247–260.

(93) Wang, L.-P.; Martinez, T. J.; Pande, V. S. Building Force Fields: An Automatic, Systematic, and Reproducible Approach. *J. Phys. Chem. Lett.* **2014**, *5*, 1885–1891.

(94) Bucsiová, L.; Hrdlovic, P. Medium Effect of Polymer Matrices on Spectral Properties of 4-Aminophthalimide and 4-Dimethylaminophthalimide. *J. Macromol. Sci. A* **2007**, *44*, 1047–1053.

(95) Reichardt, C. Solvatochromic dyes as solvent polarity indicators. *Chem. Rev.* **1994**, *94*, 2319–2358.

(96) Mayer, U.; Gutmann, V.; Gerger, W. The acceptor number—A quantitative empirical parameter for the electrophilic properties of solvents. *Monatsh. Chem.* **1975**, *106*, 1235–1257.

(97) Bayly, C. I.; Cieplak, P.; Cornell, W.; Kollman, P. A. A well-behaved electrostatic potential based method using charge restraints for deriving atomic charges: the RESP model. *J. Phys. Chem.* **1993**, *97*, 10269–10280.

(98) Jorgensen, W. L.; Chandrasekhar, J.; Madura, J. D.; Impey, R. W.; Klein, M. L. Comparison of simple potential functions for simulating liquid water. *J. Chem. Phys.* **1983**, *79*, 926–935.

(99) Novaki, L. P.; El Seoud, O. A. Solvatochromism in pure solvents: Effects of the molecular structure of the probe. *Berichte der Bunsengesellschaft für physikalische Chemie* **1996**, *100*, 648–655.

TOC graphic

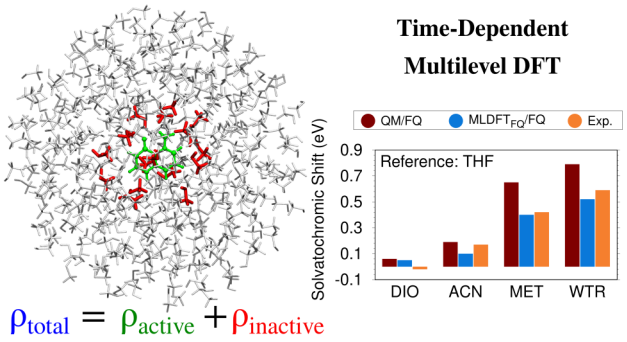
Time-Dependent
Multilevel DFT
QM/FQ
MLDFT$_{FQ}$/FQ
Exp.
Reference: THF
Solvatochromic Shift (eV)
0.9
0.7
0.5
0.3
0.1
-0.1
DIO
ACN
MET
WTR
$\rho_{total} = \rho_{active} + \rho_{inactive}$